MoS_2-graphene-$CuNi_2S_4$ nanocomposite an efficient electrocatalyst for the hydrogen evolution reaction

Prashanth Shivappa Adarakatti [a], Mallappa Mahanthappa [b], Jack P. Hughes [c], Samuel J. Rowley-Neale [c,d], Graham C. Smith[e], Ashoka S [f], Craig E. Banks [c,d]

[a] *Solid State and Structural Chemistry Unit, Indian Institute of Science, Bengaluru, 560012, India*

[b] *Department of Chemistry, School of Chemical Sciences, REVA University, Bengaluru, 560064, India*

[c] *Faculty of Science and Engineering, School of Science and the Environment, Division of Chemistry and Environmental Science, Manchester Metropolitan University, Chester Street, Manchester M1 5GD, UK*

[d] *Manchester Fuel Cell Innovation Centre, Manchester Metropolitan University, Chester Street, Manchester M1 5GD, UK*

[e] *Faculty of Science and Engineering, University of Chester, Thornton Science Park, Pool Lane, Ince, Chester CH2 4NU, UK*

[f] *Department of Chemistry, School of Engineering, Dayananda Sagar University, Bengaluru 560068, India*

Abstract

We present a facile methodology for the synthesis of a novel 2D-MoS_2, graphene and $CuNi_2S_4$ (MoS_2-g-$CuNi_2S_4$) nanocomposite that displays highly efficient electrocatalytic activity towards the production of hydrogen. The intrinsic hydrogen evolution reaction (HER) activity of MoS_2 nanosheets was significantly enhanced by increasing the affinity of the active edge sites towards H^b adsorption using transition metal (Cu and Ni_2) dopants, whilst also increasing the edge sites exposure by anchoring them to a graphene frame- work. Detailed XPS analysis reveals a higher percentage of surface exposed S at 17.04%, of which 48.83% is metal bonded S (sulfide). The resultant MoS_2-g-$CuNi_2S_4$ nanocomposites are immobilized upon screen-printed electrodes (SPEs) and exhibit a HER onset potential and Tafel slope value of -0.05 V (*vs*. RHE) and 29.3 mV dec^{-1}, respectively. These values are close to that of the polycrystalline Pt electrode (near zero potential (*vs*. RHE) and 21.0 mV dec^{-1}, respectively) and enhanced over a bare/unmodified SPE (-0.43 V (*vs*. RHE) and 149.1 mV dec^{-1}, respectively). Given the efficient, HER activity displayed by the novel MoS_2-g-$CuNi_2S_4$/SPE electrochemical platform and the comparatively low associated cost of production for this nanocomposite, it has potential to be a cost-effective alternative to Pt within electrolyser technologies.

Introduction

A plethora of emergent low polluting energy generation technologies rely upon hydrogen gas as a fuel source [42], which has created an impetus for clean hydrogen generation techniques to be developed. A prominent method for clean hydrogen generation is the Hydrogen Evolution Reaction (HER); ($2H^+ + 2e^- \rightarrow H_2$), which is the cathodic reaction within an electrolyser [1]. The power necessary to operate an electrolyser could feasibly be drawn from renewable sources, making it a "cleaner" fuel source compared to its fossil fuel (FF) counterparts [37]. A limiting factor to the ubiquitous use of electrolysers to generate hydrogen is the requirement for expensive platinum (Pt) as a catalyst for the HER [18,23,36]. Much of the research dedicated to finding an alternative to Pt has focused upon the di-chalcogenides, particularly MoS_2 based materials (see Table 1) [36], as 2D-MoS_2 nanosheets have been shown to be effective at lowering the HER onset potential and increasing the achievable current density, whilst typically being composed of significantly cheaper and more earth abundant elements [9,22,24]. For example a study by Ruiz et al. [40] utilized a chemical vapor deposition (CVD) technique to grow vertically aligned MoS_2 on a gold foil and demonstrated how the optimized (prepared at 600 ^{o}C) MoS_2 film, when used as an electrode, achieved a current density of 10 mA cm^{-2} by −0.355 V (*vs.* saturated calomel electrode (SCE)). Whilst being *ca*. −0.250 V (*vs.* SCE) more electronegative than the optimal value of Pt, it was significantly less electronegative than the values reported by Rowley-Neale et al. [36] for unmodified traditional carbon-based electrodes (boron doped diamond, edge-plane pyrolytic graphite, glassy carbon and screen-printed electrodes (SPE)).

There are a wide variety of studies within the literature, which demonstrate the capability of an MoS_2 based material to act as an efficient electrocatalyst towards the HER, however few reports show any form of catalyst that can display equivalent HER activity to Pt based electrocatalysts. In order to narrow the potential gap between the HER onset potentials of MoS_2 and Pt based catalysts, numerous studies have utilized MoS_2 nanosheets as a dopant framework in order to fabricate electrocatalysts that show more comparable HER activity to Pt. One such study by Shi et al. [43] found that Zinc (Zn) doped MoS_2 (Zn-MoS_2) when drop-cast onto a GC electrode exhibited greater HER catalysis than undoped MoS_2, with a HER onset potential of −0.13 V (*vs.* reversible hydrogen electrode (RHE)) and a Tafel slope of 51 mV dec^{-1} compared to −1.4 V (*vs.* RHE) and 101 mV dec^{-1} for undoped MoS_2 nanosheets. Shi and coworkers [43] attributed the increased HER activity to a synergistic electron (energy level matching) and morphological effect (increase in the number of exposed active edge sites) between the Zn and the MoS_2 nanosheets.

HER catalysis is thought to predominately occur at the MoS_2 nanosheets edge sites, in particular the exposed Sulfur atoms, which have an affinity towards H^+ adsorption due to a density functional theory predicting a binding energy of þ0.08 eV [24]. In contrast to this, the basal sites are relatively inert and show little catalytic activity [53], consequently the bulk of the material can be considered electrocatalytically inert [8]. Efforts to maximize the ratio of edge sites to basal sites of a given MoS_2 based material would therefore yield a more effective HER catalyst. Previous studies have shown that hybridizing an electrocatalyst with a graphitic material (*e.g.* reduced graphene oxide) offers a beneficial morphology (an increased number of exposed active sites) leading to increased catalysis [26]. Hybridization in this manner has the additional benefit of improving charge transfer and conductivity for the entire system and notably, the electrocatalytic sites [13].

Catalyst	Supporting Electrode	Loading	Deposition Technique	Electrolyte	HER onset (V)	Tafel Slope ($mV\ dec^{-1}$)	Reference
CD/MoS_2	GC	–	Drop-cast	0.5 M H_2SO_4	ca. − 0.50 (vs. RHE)	22	[7]
P-doped MoS_2	GC	0.32 mg cm^{-2}	Drop-cast	0.5 M H_2SO_4	− 0.02 (vs. RHE)	34	[30]
MoS_2–Ni_3S_2 H	NF	–	Chemical synthesis	1.0 M KOH	− 0.04 (vs. RHE)	61	[52]
MoS_2/C*	SPE	252.80 μg cm^{-2}	Drop-cast	0.5 M H_2SO_4	− 0.44 (vs. SCE)	43	[38]
MoS_2-PB/NG	GC	5 μL	Drop-cast	0.5 M H_2SO_4	− 0.08 (vs. RHE)	62	[55]
MoS_2	GC	0.24 mg cm^{-2}	Drop-cast	0.1 M H_2SO_4	− 0.12 (vs. RHE)	78	[29]
Ni–MoS_2	CC	–	Chemical synthesis	1.0 M KOH	− 0.10 (vs. RHE)	75	[48]
Ni–MoS_2	CC	–	Chemical synthesis	0.5 M H_2SO_4	− 0.11 (vs. RHE)	74	[48]
CuNi–P–MoS_2	NFL	–	Chemical synthesis	0.5 M H_2SO_4	− 0.23 (vs. RHE)	61	[2]
$NiCo_2S_4/MoS_2$	NF	3.00 mg cm^{-2}	Chemical synthesis	0.1 M KCl	− 0.40 (vs. RHE)	–	[19]
MoS_2–ZnO–Ni	NF	–	Chemical synthesis	1.0 M KOH	− 0.13 (vs. RHE)	78	[51]
MoS_2–NiS	GC	0.20 mg cm^{-2}	Drop-cast	1.0 M KOH	− 0.08 (vs. RHE)	66	[46]
DAC/MoS_2	GC	2–5 mg cm^{-2}	Drop-cast	0.5 M H_2SO_4	− 0.09 (vs. RHE)	84	[41]
A-MoS_2	GC	–	Drop-cast	2 M HNO_3	− 0.08 (vs. RHE)	97	[54]
rGO-MoS_2	GC	–	Drop-cast	0.5 M H_2SO_4	− 0.15 (vs. RHE)	36	[17]
rGO-MoS_2	GC	20 μg	Drop-cast	0.5 M H_2SO_4	− 0.13 (vs. RHE)	75	[32]
$MoS_2/MoSe_2$	CF	–	Chemical synthesis	0.5 M H_2SO_4	− 0.16 (vs. RHE)	61	[27]
MoS_2	GC	–	Drop-cast	0.5 M H_2SO_4	− 0.19 (vs. RHE)	45	[47]
MoS_2	GC	10 μL	Drop-cast	0.5 M H_2SO_4	− 0.23 (vs. RHE)	–	[35]
MoS_2 NSs	GC	285 μg cm^{-2}	Drop-cast	0.5 M H_2SO_4	ca. − 0.04 (vs. RHE)	68	[50]
V, N − MoS2/rGO	GC	5 μL	Drop-cast	0.5 M H_2SO_4	ca. − 0.03 (vs. RHE)	41	[16]
O–MoS2/G	GC	5 μL	Drop-cast	0.5 M H_2SO_4	− 0.12 (vs. RHE)	51	[15]
MoS_2-G	GC	5 μL	Drop-cast	0.5 M H_2SO_4	− 0.11 (vs. RHE)	47	[56]
MoS_2-g-$CuNi_2S_4$	SPE	0.30 mg cm^{-2}	Drop-cast	0.5 M H_2SO_4	− 0.05 (vs. RHE)	29	This work

Key: CD/MoS_2; carbon nanodot MoS_2 ensembles, GC; glassy carbon, –; no value given, RHE; reversible hydrogen electrode, P; phosphorus, NF; nickel foam, H; heteronanorods *: produced by magnetron sputtering MoS_2 onto a nanocarbon substrate, SPE; screen-printed electrode, SCE; saturated calomel electrode, NC; nanocubes, MoS_2-PB/NG; $Fe_4[Fe(CN)_6]_3$ NC with MoS_2 N-doped on graphene; CC; Carbon cloth, NFL; Nickel foil, DAC; Defective activated carbon A-MoS_2; Acid engineered, rGO; Reduced graphene oxide, CF: Carbon fibre, NSs; nanosheets, V; Vanadium, N; Nitrogen, O; Oxygen.

Table 1: Comparison Table showing the HER activity of MoS_2 and MoS_2 containing compounds.

Given the above, there are two major factors that should be considered in research focused on optimizing HER catalysis of MoS_2 containing materials. The first being: increasing the affinity of active sites towards H^+ adsorption and thus their ability to catalyze the HER. Secondly: maximizing the ratio of exposed active edge sites to inert basal sites, which will in- crease the density of sites enabling catalysis. In order to tackle both of these challenges we present a novel methodology for doping MoS_2 with transition metals (Cu and Ni) in order to increase the electron density at the electrocatalytically active edge sites and therefore improve their HER activity, whilst increasing the exposure of these sites by anchoring them to a graphene framework. The novel MoS_2-graphene-$CuNi_2S_4$ (MoS_2-g-$CuNi_2S_4$) nanocomposite is electrically wired *via* immobilization upon SPEs and experimentally explored towards the HER where it exhibits highly efficient HER catalysis.

Experimental

Chemicals

The MoS_2-g-$CuNi_2S_4$ nanocomposite precursors utilized in this study were, $Cu(NO_3)_2.6H_2O$, $Ni(NO_3)_2.6H_2O$, thiourea, MoS_2, graphite powder (30 mm) and polyvinylpyrrolidone. All of precursors were purchased from Sigma Aldrich, Merck and Sd-fine chemical PVT Ltd, respectively and used without further purification. All solutions were prepared with doubly distilled water (18.2 MU cm^{-1}) and were vigorously degassed prior to electrochemical measurements with high purity, oxygen free, nitrogen. All experiments were performed in 0.5 M H_2SO_4 in order to replicate the conditions found within an acidic proton exchange membrane fuel cell (PEMFC) [39].

Electrochemical measurements

Electrochemical measurements were studied using a CH- Electrochemical analyzer model CHI 6039E (USA). Measurements were carried out using a typical three electrode system with a nickel wire counter and a reversible hydrogen electrode (RHE) reference electrode. The working electrodes are screen-printed graphite macro electrodes (SPEs) comprising a 3.1 mm diameter working area. The SPEs were fabricated in-house with the appropriate stencils using a DEK 248 screen-printing machine (DEK, Weymouth, U.K.) [11]. The fabrication of the SPEs has been extensively described in previous publications [39], however it is repeated within the supporting information for clarity.

Synthesis of MoS_2-g-$CuNi_2S_4$ nanocomposite

The MoS_2-g-$CuNi_2S_4$ nanocomposites were synthesized by chemical exfoliation where graphite powder (120 mg) (<20 mm) and MoS_2 powder were dispersed in a solvent mixture of iso-propanol/water (V/V = 1:1). In the process of preparation, isopropanol intercalates in the layer structure of graphite where under hydrothermal conditions the graphite layers cleave and thereby result in the formation of graphene sheets. Following this, 1 mM of $Cu(NO_3)_2.6H_2O$, 2 mM $Ni(NO_3)_2.6H_2O$, PVP and thiourea were added to 12.5 mL of the graphene/MoS_2 solution at a concentration of 1, 2, 1 and 9 mM, respectively. Next, 1 mL of ammonia was added drop wise to the solution under continuous stirring. The solution mixture was then transferred into a Teflon lined autoclave, sealed and heated, at 180 ^{O}C, for 24 h. The obtained black solid product was filtered, washed with water and ethanol several times then left to dry in a hot air oven, at 80 ^{O} C, for 12 h. For comparative purposes $CuN_{i2}S_4$, g-$CuNi_2S_4$ and MoS_2-$CuNi_2S_4$ were fabricated in the same manner and electrochemically explored towards the HER.

Instrumentation

The phase transition, purity and crystal structure of the synthesized compounds were analyzed by a PAnalytical X'pert PRO powder X-ray powder diffractometer (XRD) equipped with Ni-filtrated Cu Ka radiation (40 kV, 200 mA). The composition and functional groups present in the as prepared catalyst was monitored by Agilent carry-630 Fourier transform infrared (FT-IR) spectroscopy over the range of 400-4000 cm^{-1}. Raman Spectroscopy was performed using a 'Renishaw InVia' spectrometer equipped with a confocal microscope (x 50 objective) and an argon laser (514.3 nm excitation). Measurements were performed at a very low laser power level (0.8 mW) to avoid any heating effects. The optical absorbance spectra of as prepared HER catalyst was monitored by UV-visible absorption spectroscopy (UV-1800, Shimadzu, Japan). The morphology, composition, size and crystallinity of the as prepared HER catalyst was analyzed by scanning electron microscope (SEM) using a JEOL JSM-5600LV model SEM. Transmission electron microscopy (TEM) images were obtained using a 200 kV primary beam under conventional bright-field conditions with an energy dispersive X-ray microanalysis (EDX) package. The MoS_2-g-$CuNi_2S_4$ sample was dispersed onto a holey-carbon film supported on a 300 mesh Cu TEM grid. X-ray photoelectron (XPS) analysis of the samples was performed using a bespoke ultra-high vacuum system fitted with a Specs GmbH Focus 500 monochromated Al Ka X-ray source, Specs GmbH Phoibos 150 mm mean radius hemispherical analyser with 9-channeltron detection, and a Specs GmbH FG20 charge neutralising electron gun. The Al monochromator source was used to generate a survey scan and higher resolution scans over C 1s, O 1s, Cu 2p, Ni, 2p, N 1s, S 2p and, where detected, Mo 3d photoelectron lines. A representative area approximately 1.4 mm in diameter over the center of each sample was analysed.

Electrode preparation

Following the synthesis of the nanocomposites, their HER activity was electrochemically explored. This was done by dispersing 5 mg of the catalyst and 5 wt% nafion into a solution of water and ethanol, the solution was ultra-sonicated for 30 min to ensure it was homogenous. 5 mL of this suspension was then drop-caste (where an aliquot of the given solution is deposited onto the working area of an SPE, using a manual micro-pipette). This resulted in a surface coverage of *ca*. 0.3 mg cm^{-2} MoS_2-g-$CuNi_2S_4$. The electrode was then air dried for 30 min to ensure evaporation of the water and ethanol. The prepared electrode was then ready for use.

Results and discussion

Physicochemical characterization of the nanocomposites

A thorough physicochemical analysis of the novel synthesized MoS_2-g-$CuNi_2S_4$ nanocomposite, was performed using FT-IR, Raman spectroscopy, SEM, TEM, TGA, EDX, XRD and XPS.

TEM imaging of the MoS_2-g-$CuNi_2S_4$ nanocomposite is shown in Fig. 1 showing that the MoS_2-g-$CuNi_2S_4$ nanocomposite had an average diameter of *ca.* 50 nm, however there are signs of agglomeration of the new particles. Note that Fig. 1(B) has five separate sites identified which are the locations of elemental composition analysis *via* EDX, the results of which are prescribed within in Table S1. Note that the presence of all the expected elementals, and there is a higher than expected percentage of Cu observed, which is likely a result of the use of a Cu supporting grid. EDX mapping of a MoS_2-g-$CuNi_2S_4$ flake (see ESI Fig. S1) showed uniform distribution S, Cu, Ni, Mo and O upon the flakes surface. The FTIR spectrum of the MoS_2-g-$CuNi_2S_4$ nanocomposite is given in Fig. 2(A). The majority of peaks between 1000 and 4000 cm^{-1} can be ascribed to graphitic components, for example the peaks at 1609 and 2911 cm^{-1} are characteristic of sp^2 hybridized carbon and hydroxyl groups, respectively [45]. Note the peak at 3434 cm^{-1} is the characteristic band of O-H [57]. The weak observable peak at 479 is likely due to Mo-S vibration [31]. Raman spectroscopy was also performed on the MoS_2-g- $CuNi_2S_4$ with the obtained spectrum being shown in Fig. 2(B). Vibrational bands (VB) at *ca.* 378 and 403 cm^{-1}, which correspond to the E^1_{2g} and A_{1g}, of MoS , can be observed [25]. Additionally VBs at *ca*. 1360 and 1578 cm^{-1} are observed, these correspond to the D and G bands of a graphitic material [6,34]. Finally, the presence of a peak at *ca*. 2713 cm^{-1} (2D band) is also characteristic of graphitic materials [6,10], thus confirming the presence of high quality few layer graphene and MoS_2 [21,33]. The XRD profile of the MoS_2-g-$CuNi_2S_4$ nanocomposite is shown in Fig. 2(D). Except for the indexed MoS_2 peaks (corresponding to JCPDS No. 37-1492), all of the other diffraction peaks can be ascribed to the cubic phase of $CuNi_2S_4$ (JCPDS No. 24-334). For instance, the typical diffraction peaks of (311), (400), (511), and (440) diffraction planes can be clearly indexed at 31.4°, 38.2°, 50.1°, and 55.1°, respectively. No obvious peaks from other phases such as CuS, NiS, or organic compounds related to the precursors were detected. Furthermore, graphene/graphite peak (002) at 26.5° [33], in the XRD patterns as well as the characteristic (002) peak for MoS_2 at 14.2° [20]. It was important to determine the elemental composition of each of the nanocomposites, therefore XPS analysis was performed on the samples. A typical survey spectra of the MoS_2-g-$CuNi_2S_4$ is shown in Fig. 2(C), where all the expected elements can be observed as well as low levels of N and Si (the presence of N is likely due to atmospheric contamination, whilst the Si can be attributed to the Si containing adhesive tape used to fix the samples during analysis). The full elemental composition of each composite material is shown within Table 2. Table 3 gives the results of the quantification analysis of all the synthesized nanocomposites and ESI Fig. S2 displays high resolution XPS spectra of the Mo, S, C, O, Cu and Ni components for the MoS_2-g-$CuNi_2S_4$ nanocomposite. Note that further XPS analysis is described later within the manuscript in order to provide insights into the substantial HER activity observed by the MoS_2-g-$CuNi_2S_4$. Lastly, thermogravimetric analysis assessed the thermal stability of the MoS_2-g-$CuNi_2S_4$. It is clear from

inspection of ESI Fig. 3 that the nanocomposite was stable until *ca.* 200 ^{o} C after which the MoS_2-$CuNi_2S_4$ exhibited a rapid and uniform decomposition to *ca.* 75% by 900 ^{o}C. The average working temperature of a proton exchange membrane electrolyser is between 50 and 80 ^{o}C [14], so MoS_2-g-$CuNi_2S_4$ could maintain its composition within an operating electrolyser. Given the thorough physicochemical analysis given above the MoS_2-g- $CuNi_2S_4$ nanocomposite is shown to be of high purity and crystallinity.

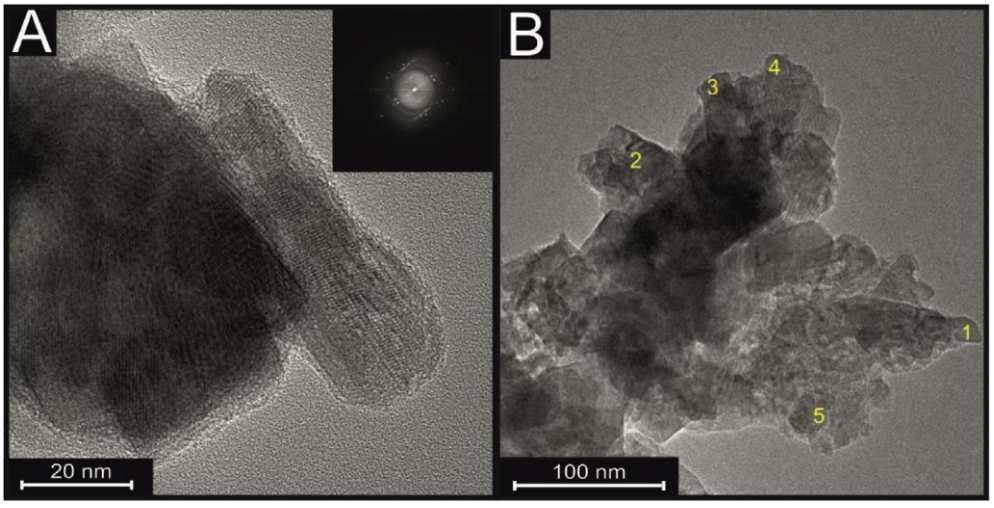

Fig. 1: Transmission electron microscopy (TEM) MoS_2-g-$CuNi_2S_4$ nanocomposite. Five sites of energy-dispersive X-ray (EDX) analysis are shown in (B) with the corresponding elemental compositions given in Table S1.

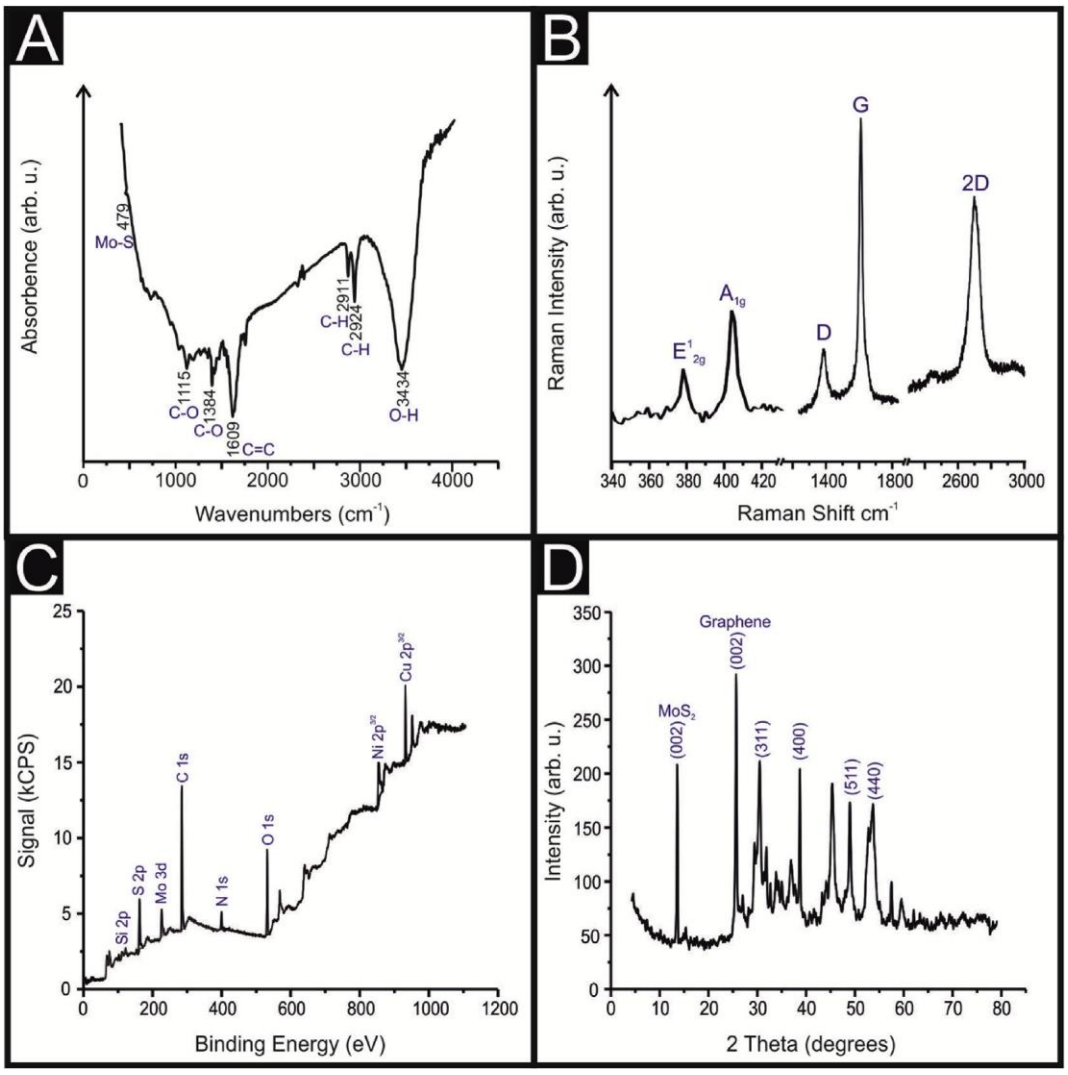

Fig. 2: Physicochemical characterisation of the synthesized MoS_2-g-$CuNi_2S_4$ nanocomposites with FTIR (A), Raman (B), XPS (C) and XRD (D).

Table 2: XPS elemental quantification of the $CuNi_2S_4$, g- $CuNi_2S_4$, MoS_2-$CuNi_2S_4$ and MoS_2-g-$CuNi_2S_4$ nanocomposites.

Element Composition (%)	$CuNi_2S_4$	g-$CuNi_2S_4$	MoS_2e $CuNi_2S_4$	MoS_2-g- $CuNi_2S_4$
Cu $2p_{3/2}$	3.14	2.33	2.06	2.72
Ni $2p_{3/2}$	5.72	5.37	4.11	4.41
O 1s	29.95	18.11	15.54	13.30
N 1s	7.88	3.97	2.73	4.28
C 1s	33.97	58.74	57.33	57.06
S 2p	19.33	11.48	15.95	17.04
Mo 3d	e	e	2.28	1.19

Application of the MoS_2-g-$CuNi_2S_4$/SPEs towards the HER

Initially it was important to benchmark the electrochemical behavior of a bare/unmodified SPE and a polystalline platinum (Pt) electrode towards the HER in 0.5 M H_2SO_4. Fig. 3(A) shows the linear sweep voltammetry (LSV) obtained for a bare/un- modified SPE and Pt electrode as well as for the $CuNi_2S_4$/SPE, g-$CuNi_2S_4$/SPE, MoS_2e$CuNi_2S_4$/SPE and MoS_2-g-$CuNi_2S_4$/SPEs. The bare/unmodified SPE had an onset potential of e 0.43 V (*vs.* RHE), as expected this is far more electronegative than the optimal HER onset potential for Pt. Note that within this study the HER onset potential is determined as the potential when the current deviates from the background current by 25 mA cm^{-2}. From inspection of Fig. 3(A) it is clear that upon immobilization of all of the nanocomposites onto an SPE there is a decrease in the electronegativity of the HER onset potential, with the $CuNi_2S_4$ /SPE, g-$CuNi_2S_4$/SPE, MoS_2-$CuNi_2S_4$/SPE and MoS_2-g-$CuNi_2S_4$/SPE exhibiting HER onset potentials of -0.41, - 0.15, - 0.13 and - 0.05 V (*vs.* RHE), respectively. It is also worth noting there is a corresponding increase in the achievable current densities with the MoS_2-g-$CuNi_2S_4$/SPEs reaching 10 mA cm^{-2} by - 0.12 V (*vs.* RHE). The intrinsic electrocatalysis of the $CuNi_2S_4$/SPE, g-$CuNi_2S_4$/SPE, MoS_2-$CuNi_2S_4$/SPE and MoS_2-g-$CuNi_2S_4$/SPE was deduced by means of a H_2 Turn over Frequency (ToF) calculation. These ToF calculations are presented in the supplementary information (see ESI Figs. 4 and 5). The $CuNi_2S_4$/SPE, g-$CuNi_2S_4$/SPE, MoS_2-$CuNi_2S_4$/SPE and MoS_2-g-$CuNi_2S_4$/SPE exhibited ToF values of 0.083, 0.19, 0.53 and 0.73H_2 s^{-1}, respectively. In comparison of the nanocomposites synthesized, the MoS_2-g-$CuNi_2S_4$/SPE displays the most optimal HER activity with a HER onset potential close to that of Pt. This is likely a result of MoS_2-g-$CuNi_2S_4$ having the largest number of exposed active edge sites for H^+ adsorption as a result of the graphene acting as a framework for optimal exhibition of the sulfur edge sites of MoS_2 and $CuNi_2S_4$ in addition to the electrocatalytically active functional moieties in graphene. Additionally, the graphene acted to increase the electroconductivity, whilst the interface in MoS_2-g- $CuNi_2S_4$ facilitates the electron transfer during electrocatalysis.

Table 3: XPS quantification of sulfur containing components of the $CuNi_2S_4$, g-$CuNi_2S_4$, MoS_2eCuNi_2S_4 and MoS_2-g- $CuNi_2S_4$ nanocomposites.

Sample	Atom % S	Binding energy of $2p_3$ (eV)	% of S total	Atom %	Chemical state
$CuNi_2S_4$	19.33	161.1	36.69	7.09	metal-S [12]
		162.5	22.12	4.28	metal bonded organic S [12]
		164.6	5.89	1.14	*e.g.* metal-S-C organic S *e.g.* CeS [5]
		168.5	35.3	6.82	sulfate, SO^{2-} [3]
graphene-$CuNi_2S_4$	11.48	161.9	31.81	3.65	metal-S
		163.1	43.86	5.04	metal bonded organic S *e.g.* metal-S-C organic S
		164.4	13.86	1.59	*e.g.* CeS
		168.4	10.48	1.2	sulfate, SO^{2-}_4
MoS_2eCuNi_2S_4	15.95	161.4	40.02	6.38	metal-S
		162.6	45.56	7.27	metal bonded organic S
		164.4	6.77	1.08	*e.g.* metal-S-C organic S *e.g.* CeS
		167.7	6.66	1.06	sulfate, SO^{2-}_4
MoS_2-g-$CuNi_2S_4$	17.04	161.5	48.83	8.32	metal-S
		162.7	36.55	6.23	metal bonded organic S
		164.6	6.57	1.12	*e.g.* metal-S-C organic S *e.g.* CeS
		168.4	8.04	1.37	sulfate, SO^{2-}_4

Tafel analysis

In order to determine whether the increased HER activity observed from an SPE post nanocomposite immobilization was as a result of the catalyst enabling a change in the reaction mechanism, Tafel analysis was performed. The activity of a HER catalyst is related to the kinetic barrier of the rate- determining hydrogen evolution pathway. According to the literature, HER mechanism involves three possible rate limiting steps, those being: (i) initial H^+ adsorption step, known as the Volmer step,

$$\textbf{Volmer}: H_3O^+ + \text{Catalyst} + e^- \rightarrow H_{ads} + H_2O\,(l);\ 2.\frac{303RT}{\alpha F} \approx 120mV$$

(ii) Volmer-Heyrosky discharge step

$$\textbf{Heyrovsky}: H_3O^+ + H_{ads} + e^- \rightarrow H_2\,(g) + H_2O\,(l);\ 2.\frac{303RT}{(1+2)F} \approx 40mV$$

(iii) Volmer-Tafel discharge step:

$$\textbf{Tafel}: H_{ads} + H_{ads} \rightarrow H_2\,(g);\ 2.\frac{303RT}{2F} \approx 30mV$$

Where the transfer coefficient (α) is 0.5, *F* is the Faraday constant, *R* is the universal gas constant and *T* is the temperature at which the electrochemical experiment was performed (298 K). Tafel analysis was performed on the Faradaic section of the LSVs shown in Fig. 3(A) with the resultant Tafel slopes being given in Fig. 3(B). The determined Tafel slopes for the bare/unmodified SPE and Pt electrodes were 149.1 and 21.0 mV dec^{-1}, respectively, these values correspond to those reported in previous literature. The determined Tafel values suggest that the rate limiting step of the HER mechanism on a bare/ unmodified SPE is the Volmer step whilst a Pt electrode allows the HER to occur *via* the desirable Volmer-Tafel mechanism. The Tafel slope values obtained for the $CuNi_2S_4$/SPE, g-$CuNi_2S_4$/SPE, MoS_2-$CuNi_2S_4$/SPE and MoS_2-g-$CuNi_2S_4$/SPE CuNi S /SPE, MoS eCuNi S /SPE and MoS -g-CuNi S /SPEs were 147.3, 111.8, 44.7 and 29.3 mV dec^{-1} respectively. Interpretation of these Tafel values, reveals that for the $CuNi_2S_4$/ SPE and g-$CuNi_2S_4$/SPE there is not an alteration in the reaction mechanism with the Volmer adsorption step still being the rate limiting step. However, for the MoS_2eCuNi$_2S_4$/SPE and MoS_2-g-$CuNi_2S_4$/SPEs there is a significant increase in the current density resulting in the Tafel discharge step becoming the rate limiting step. The smallest Tafel value was recorded for the MoS_2-g-$CuNi_2S_4$/SPE, this suggests that MoS_2-g- $CuNi_2S_4$ substantially enhances the HER capability of the SPE platform to close to that of a Pt electrode. The data presented above clearly shows that hybridization of MoS_2 with graphene and $CuNi_2S_4$ significantly improves HER catalysis. The literature suggests that it is the exposed sulfur atoms located at the MoS_2 nanosheets edge sites that produce HER activity, it was therefore vital that we investigate the chemical changes responsible for the reported increase in catalysis. A detailed quantitative XPS analysis of the S components for each of the nanocomposites was performed. The obtained high resolution S 2p spectra (See ESI Fig. S2) were complex in shape, exhibiting good evidence for 4 separate chemical environments. S 2p peaks were fitted with multiple sets of $2p_{3/2}$-$2p_{1/2}$ doublets. In each case, the two components of the doublet had to be constrained to the same width and line shape, the area ratio is constrained so that the $2p_{1/2}$ component is 50% of the intensity of the $2p_{3/2}$ component (as expected from orbital occupancies), and the two components are constrained to be separated by 1.13 eV. The 4 separate chemical environments for S were: Metal-bonded S *e.g.* metal sulfide bonds such as Cu-S, Ni-S, Mo-S, typically 161-162 eV, Metal bonded to organic S, typically 162.5-163 eV, organic (carbon bonded) sulfur, typically 164.4-164.6 eV, and oxidized S *e.g.* as sulfate, typically 168.4-168.5 eV. The relative percentage quantity of each of these components with the four nanocomposites is summarized in Table 3. It is evident that there is a strong positive correlation between atomic percentage of S (especially metal bonded S) and electrocatalytic activity towards the HER for the MoS_2-g-$CuNi_2S_4$, MoS_2-$CuNi_2S_4$ and g- $CuNi_2S_4$. As shown by analysis of the MoS_2-g-$CuNi_2S_4$, which displayed the greatest HER catalysis and had the highest atomic percentage of S at 17.04%, of which 48.83% was metal bonded S (*the highest percentage recorded for any of the nano- composites*). Note that $CuNi_2S_4$ has the highest atomic percentage of S of all four nanocomposites and a higher % of metal bonded S than MoS_2- $CuNi_2S_4$ or g-$CuNi_2S_4$, however it displays the least amount of HER catalytic activity. We summarize this to the lack of Mo, and therefore the lack of Mo-S sulfides, within the $CuNi_2S_4$. So whilst there is a relatively high % of metal-S bonds these are likely Cu-S and Ni-S, therefore suggesting that the S present is not in a chemical environment complimentary to HER catalysis.

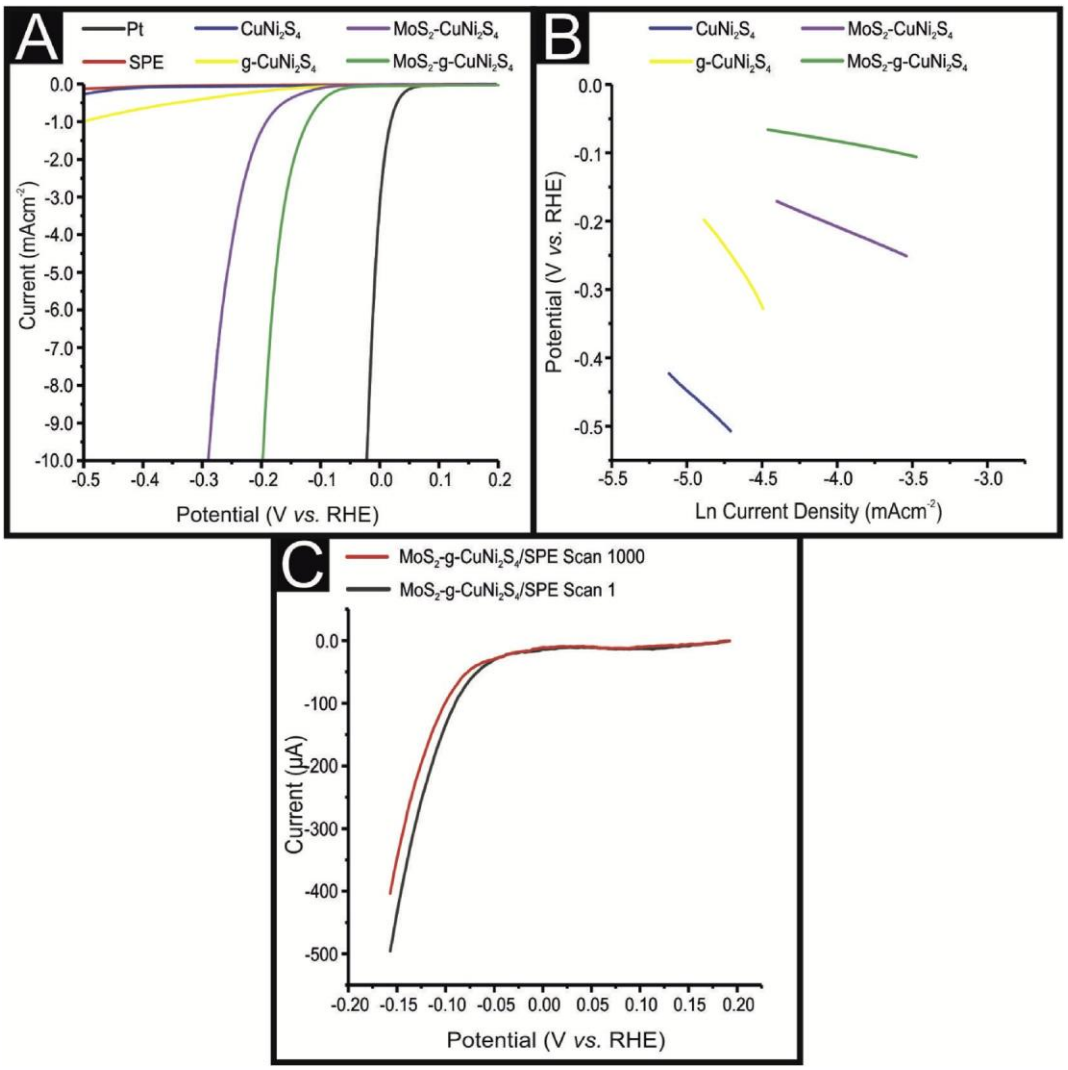

Fig. 3: (A) Linear sweep voltammetry of unmodified and various modified electrodes showing HER activity of a bare/ unmodified SPE, polycrystalline platinum electrode, $CuNi_2S_4$/SPE, g-$CuNi_2S_4$/SPE, MoS_2-$CuNi_2S_4$/SPE and MoS_2-g-$CuNi_2S_4$/SPE, Solution composition: 0.5 M H_2SO_4; Scan rate: 20 mVs^{-1} (vs. RHE). (B) Tafel slopes corresponding to the Faradaic regions of the LSVs shown in (A). (C) Cyclic stability examination of a 10% MoS_2-g-$CuNi_2S_4$/SPE via LSV (scan rate: 100 mV s^{-1} (vs. RHE)) was performed between the potential range of 0 to −0.35 V, repeated for 1000 cycles, this figure shows the first scan (black line), 1000th (red line).

The as prepared materials $CuNi_2S_4$, g-$CuNi_2S_4$, MoS_2-$CuNi_2S_4$ and MoS_2-g-$CuNi_2S_4$ were further examined using electrochemical impedance spectroscopy (EIS) in order to determine the impedance of the interface system. EIS is a useful technique to characterize interface reactions and electrode kinetics in HER. ESI Fig. S6 shows the Nyquist plots recorded for all of the nanocomposite modified SPEs using an overpotential of 150 mV (*vs*. RHE). The MoS_2-g-$CuNi_2S_4$ exhibited the smallest Rct at 10.08 kΩ compared to 44.35, 39.27 kΩ and 112.0 kΩ for the $CuNi_2S_4$, g-$CuNi_2S_4$ and MoS_2-$CuNi_2S_4$, respectively. The EIS data presented above supports the prior inference that MoS_2-g-$CuNi_2S_4$ is the most effective electrocatalyst for the HER as it displayed the fastest rate of reaction. Lastly it was essential to assess the stability, of the MoS_2-g-$CuNi_2S_4$, at catalyzing the HER, as longevity and durability are important considerations if catalyst is to be implemented in an industrial application [28,44,49]. The stability of the MoS_2-g-$CuNi_2S_4$/SPEs towards HER has been tested by performing 1000 repeat cycling voltammograms (See Fig. 3(C)) as well as performing chronoamperometry for 36,000 s (see supporting information and ESI Fig. 7). A slight decrease in catalytic activity of MoS_2-g-$CuNi_2S_4$/SPE is observed over the course of the 1000

scans, with the current density at −0.10 V decreasing from −134 μA for the first scan to 98 μA for the 1000th scan. The observed decrease in HER catalysis over for the course of 1000 CVs is likely a result of the MoS_2-g-$CuNi_2S_4$ delaminating from the supporting SPEs surface due to hydrogen bubbling from the surface as the HER occurs [4].

Conclusions

The synthesis of a novel MoS_2-g-$CuNi_2S_4$ nanocomposite that displays remarkable HER catalysis upon immobilization to a SPE, has been reported. The intrinsic HER activity of MoS_2 was improved by increasing the affinity of the active edge sites, of the MoS_2 nanosheets, for H^+ adsorption using transition metal (Cu and Ni) dopants, whilst also increasing the edge sites exposure by anchoring them to a graphene framework. Through a detailed XPS analysis, we demonstrated that the synthesis process, in particular hybridizing the MoS_2 with graphene, increases the percentage of electrocatalytic surface exposed S as well as the proportion of metal bonded S from 15.95% to 40.02%, respectively for the MoS_2-$CuNi_2S_4$ nanocomposite to 17.04% and 48.83%, respectively for the MoS_2-g-$CuNi_2S_4$ nanocomposite. The optimized MoS_2-g-$CuNi_2S_4$ electrocatalyst when immobilized upon SPEs display near Pt HER activity with a HER onset potential and Tafel slope value of -0.05 V (*vs*. RHE) and 29.3 mV dec^{-1}, respectively. These values are far greater than those of a bare/unmodified SPE (-0.43 V (*vs*. RHE) and 149.1 mV dec^{-1}), and the equivalent masses of the other synthesized nanocomposites upon an SPE (($CuNi_2S$ (-0.41 V (*vs*. RHE) and 147.3 mV dec^{-1}), g-$CuNi_2S_4$ (-0.15 V (*vs*. RHE) and 111.8 mV dec^{-1}) and MoS_2-$CuNi_2S_4$. We have provided insights into the synthesis of a novel HER catalyst (MoS_2-g- $CuNi_2S_4$), which exhibits a near Pt electrocatalytic activity towards the HER. Clearly MoS_2-g-$CuNi_2S_4$ has the potential to act as a cost-effective alternative to Pt, when utilized as the cathodic electrocatalyst implemented within the triple phase boundary of commercial PEM electrolysers.

References

1. Ahmed A, Al-Amin AQ, Ambrose AF, et al. Hydrogen fuel and transport system: a sustainable and environmental future. Int J Hydrogen Energy 2016;41:1369-80.
2. Ahn B-W, Kim T-Y, Kim S-H, et al. Amorphous MoS2 nanosheets grown on copper@nickel-phosphorous dendritic structures for hydrogen evolution reaction. Appl Surf Sci 2018;432:183-9.
3. Audi AA, Sherwood PMA. X-ray photoelectron spectroscopic studies of sulfates and bisulfates interpreted by Xa and band structure calculations. Surf Interface Anal 2000;29:265-75.
4. Benck JD, Chen Z, Kuritzky LY, et al. Amorphous molybdenum sulfide catalysts for electrochemical hydrogen production: insights into the origin of their catalytic activity. ACS Catal 2012;2:1916-23.
5. Brown JR, Kasrai M, Bancroft GM, et al. Direct identification of organic sulphur species in Rasa coal from sulphur L-edge X- ray absorption near-edge spectra. Fuel 1992;71:649-53.
6. Brownson DaC, Varey SA, Hussain F, et al. Electrochemical properties of CVD grown pristine graphene: monolayer- vs. quasi-graphene. Nanoscale 2013;6:1607-21.
7. Canton-Vitoria R, Vallan L, Urriolabeitia E, et al. Electronic interactions in illuminated carbon dot/MoS2 ensembles and electrocatalytic activity towards hydrogen evolution. Chem Eur J 2018;24:10468-74.
8. Chou SS, Sai N, Lu P, et al. Understanding catalysis in a multiphasic two-dimensional transition metal dichalcogenide. Nat Commun 2015;6:8311.
9. Escalera-Lo pez D, Niu Y, Yin J, et al. Enhancement of the hydrogen evolution reaction from Ni-MoS2 hybrid nanoclusters. ACS Catal 2016;6:6008-17.

10. Ferrari AC. Raman spectroscopy of graphene and graphite: disorder, electron-phonon coupling, doping and nonadiabatic effects. Solid State Commun 2007;143:47-57.
11. Foster CW, Kadara RO, Banks CE. Screen-printing electrochemical architectures. Germany: Springer International Publishing; 2016.
12. Gobbo P, Biesinger MC, Workentin MS. Facile synthesis of gold nanoparticle (AuNP)-carbon nanotube (CNT) hybrids through an interfacial Michael addition reaction. Chem Commun 2013;49:2831e3.
13. Gong M, Li Y, Wang H, et al. An advanced Ni-Fe layered double hydroxide electrocatalyst for water oxidation. J Am Chem Soc 2013;135:8452-5.
14. Görgün H. Dynamic modelling of a proton exchange membrane (PEM) electrolyzer. Int J Hydrogen Energy 2006;31:29e38.
15. Guo J, Li F, Sun Y, et al. Oxygen-incorporated MoS2 ultrathin nanosheets grown on graphene for efficient electrochemical hydrogen evolution. J Power Sources 2015;291:195e200.
16. Guo J, Zhang K, Sun Y, et al. Enhanced hydrogen evolution of MoS2/RGO: vanadium, nitrogen dopants triggered new active sites and expanded interlayer. Inorganic Chemistry Frontiers 2018;5:2092-9.
17. He HY, He Z, Shen Q. Efficient hydrogen evolution catalytic activity of graphene/metallic MoS_2 nanosheet heterostructures synthesized by a one-step hydrothermal process. Int J Hydrogen Energy 2018;43(48):21835-43.
18. Ji S, Yang Z, Zhang C, et al. Exfoliated MoS2 nanosheets as efficient catalysts for electrochemical hydrogen evolution. Electrochim Acta 2013;109:269-75.
19. Jia Y, Ma Y, Lin Y, et al. In-situ growth of hierarchical NiCo2S4/MoS2 nanotube arrays with excellent electrochemical performance. Electrochim Acta 2018;289:39-46.
20. Joensen P, Crozier ED, Alberding N, Frindt RF. A study of single-layer and restacked MoS2 by X-ray diffraction and X- ray absorption spectroscopy. J Phys C: Solid State Phys 1987;20:4043-53.
21. Kumar MP, Kesavan T, Kalita G, et al. On the large capacitance of nitrogen doped graphene derived by a facile route. RSC Adv 2014;4:38689-97.
22. Lazar P, Otyepka M. Role of the edge properties in the hydrogen evolution reaction on MoS2. Chem Eur J 2017;23:4863-9.
23. Lei Z, Xu S, Wu P. Ultra-thin and porous MoSe2 nanosheets: facile preparation and enhanced electrocatalytic activity towards the hydrogen evolution reaction. Phys Chem Chem Phys 2016;18:70-4.
24. Li G, Zhang D, Qiao Q, et al. All the catalytic active sites of MoS2 for hydrogen evolution. J Am Chem Soc 2016;138:16632-8.
25. Li H, Zhang Q, Yap CCR, et al. From bulk to monolayer MoS2: evolution of Raman scattering. Adv Funct Mater 2012;22:1385-90.
26. Li P, Zeng HC. Sandwich-Like nanocomposite of CoNiOx/ reduced graphene oxide for enhanced electrocatalytic water oxidation. Adv Funct Mater 2017;27:1606325.
27. Li S, Zang W, Liu X, et al. Heterojunction engineering of MoSe2/MoS2 with electronic modulation towards synergetic hydrogen evolution reaction and supercapacitance performance. Open Chem Eng J 2018.
28. Li Y, Wang H, Xie L, et al. MoS2 nanoparticles grown on graphene: an advanced catalyst for the hydrogen evolution reaction. J Am Chem Soc 2011;133:7296-9.
29. Li Z, Ma J, Zhou Y, et al. Synthesis of sulfur-rich MoS2 nanoflowers for enhanced hydrogen evolution reaction performance. Electrochim Acta 2018;283:306-12.
30. Liu P, Zhu J, Zhang J, et al. P dopants triggered new basal plane active sites and enlarged interlayer spacing in MoS2 nanosheets toward electrocatalytic hydrogen evolution. ACS Energy

Lett 2017;2:745-52.

31. Liu S, Zhang X, Shao H, et al. Preparation of MoS2 by electrospinning. Mater Lett 2012;73:223-5.
32. Liu Y, Liu J, Li Z, et al. Exfoliated MoS2 with porous graphene nanosheets for enhanced electrochemical hydrogen evolution. Int J Hydrogen Energy 2018;43:13946-52.
33. Naebe M, Wang J, Amini A, et al. Mechanical property and structure of covalent functionalised graphene/epoxy nanocomposites. Sci Rep 2014;4:4375.
34. Randviir EP, Brownson DaC, Metters JP, et al. The fabrication, characterisation and electrochemical investigation of screen-printed graphene electrodes. Phys Chem Chem Phys 2014;16:4598-611.
35. Ravikumar CH, Nair GV, Muralikrishna S, et al. Nanoflower like structures of MoSe2 and MoS2 as efficient catalysts for hydrogen evolution. Mater Lett 2018;220:133-5.
36. Rowley-Neale SJ, Brownson DaC, Smith GC, et al. 2D nanosheet molybdenum disulphide (MoS2) modified electrodes explored towards the hydrogen evolution reaction. Nanoscale 2015;7:18152-68.
37. Rowley-Neale SJ, Foster CW, Smith GC, et al. Mass-producible 2D-MoSe2 bulk modified screen-printed electrodes provide significant electrocatalytic performances towards the hydrogen evolution reaction. Sustainable Energy Fuels 2017;1:74e83.
38. Rowley-Neale SJ, Ratova M, Fugita LTN, et al. Magnetron sputter-coated nanoparticle MoS2 supported on nanocarbon: a highly efficient electrocatalyst toward the hydrogen evolution reaction. ACS Omega 2018;3:7235-42.
39. Rowley-Neale SJ, Smith GC, Banks CE. Mass-Producible 2d- MoS2-impregnated screen-printed electrodes that demonstrate efficient electrocatalysis toward the oxygen reduction reaction. ACS Appl Mater Interfaces 2017;9:22539e48.
40. Ruiz KH, Liu J, Tu R, et al. Effect of microstructure on HER catalytic properties of MoS2 vertically standing nanosheets. J Alloy Comp 2018;747:100-8.
41. Sangeetha DN, Selvakumar M. Active-defective activated carbon/MoS2 composites for supercapacitor and hydrogen evolution reactions. Appl Surf Sci 2018;453:132-40.
42. Schultz MG, Diehl T, Brasseur GP, et al. Air pollution and climate-forcing impacts of a global hydrogen economy. Science 2003;302:624-7.
43. Shi Y, Zhou Y, Yang D-R, et al. Energy level engineering of MoS2 by transition-metal doping for accelerating hydrogen evolution reaction. J Am Chem Soc 2017;139: 15479-85.
44. Shin S, Jin Z, Kwon DH, et al. High turnover frequency of hydrogen evolution reaction on amorphous MoS2 thin film directly grown by atomic layer deposition. Langmuir 2015;31:1196-202.
45. Sudesh, Kumar N, Das S, et al. Effect of graphene oxide doping on superconducting properties of bulk MgB 2. Supercond Sci Technol 2013;26:095008.
46. Tang C, Zhang H, Xu K, et al. Scalable synthesis of heterostructure molybdenum and nickel sulfides nanosheets for efficient hydrogen generation in alkaline electrolyte. Catal Today 2018;316:171-6.
47. Wan Y, Zhang Z, Xu X, et al. Engineering active edge sites of fractal-shaped single-layer MoS2 catalysts for high- efficiency hydrogen evolution. Nanomater Energy 2018;51:786-92.
48. Wang Q, Zhao ZL, Dong S, et al. Design of active nickel single- atom decorated MoS2 as a pH-universal catalyst for hydrogen evolution reaction. Nanomater Energy 2018;53:458-67.
49. Wang T, Liu L, Zhu Z, et al. Enhanced electrocatalytic activity for hydrogen evolution reaction from self-assembled monodispersed molybdenum sulfide nanoparticles on an Au electrode. Energy Environ Sci 2013;6:625-33.
50. Wu Z, Fang B, Wang Z, et al. MoS2 nanosheets: a designed structure with high active site

density for the hydrogen evolution reaction. ACS Catal 2013;3:2101-7.

51. Xu L, Wang S. A novel hierarchical MoS2-ZnO-Ni electrocatalyst prepared by electrodeposition coupling with dealloying for hydrogen evolution reaction. J Electroanal Chem 2018;808:173-9.
52. Yang Y, Zhang K, Lin H, et al. MoS2eNi3S2 heteronanorods as efficient and stable bifunctional electrocatalysts for overall water splitting. ACS Catal 2017;7:2357-66.
53. Zhang J, Wu J, Guo H, et al. Unveiling active sites for the hydrogen evolution reaction on monolayer MoS2. Adv Mater 2017;29:1701955.
54. Zhang W, Xie Z, Wu X, et al. Acid-engineered defective MoS2 as an efficient electrocatalyst for hydrogen evolution reaction. Mater Lett 2018;230:232-5.
55. Zhang X, Wu Y, Sun Y, et al. Hybrid of Fe4[Fe(CN)6]3 nanocubes and MoS2 nanosheets on nitrogen-doped graphene realizing improved electrochemical hydrogen production. Electrochim Acta 2018;263:140-6.
56. Zhang X, Zhang Q, Sun Y, et al. MoS2-graphene hybrid nanosheets constructed 3D architectures with improved electrochemical performance for lithium-ion batteries and hydrogen evolution. Electrochim Acta 2016;189:224-30.
57. Zhao J, Zhang Z, Yang S, et al. Facile synthesis of MoS2 nanosheet-silver nanoparticles composite for surface enhanced Raman scattering and electrochemical activity. J Alloy Comp 2013;559:87e91.